Ocean Engineering 253 (2022) 111304

Contents lists available at ScienceDirect

Ocean Engineering

journal homepage: www.elsevier.com/locate/oceaneng

Numerical simulation of the hydrodynamic characteristics of unmanned underwater vehicles near ice surface

Wanzhen Luo [a,b], Dapeng Jiang [a,b,**], Tiecheng Wu [a,b,*], Moyu Liu [c], Yulong Li [d]

[a] School of Ocean Engineering and Technology, Sun Yat-sen University, Zhuhai, 519000, China
[b] Southern Marine Science and Engineering Guangdong Laboratory (Zhuhai), Zhuhai, 519000, China
[c] Institute of Mechanics, Chinese Academy of Sciences, Beijing, 100190, China
[d] Technology Centre for Offshore and Marine Singapore, Singapore

ARTICLE INFO

Keywords:
Polar region
Unmanned underwater vehicle
Near ice surface
Hydrodynamic performance
Numerical simulation

ABSTRACT

In this study, the computational fluid dynamics (CFD) method is used to calculate the hydrodynamic performance of UUVs at different velocities and depths near the free surface, near the ice surface, and at an infinite depth. The resistance, lift, velocity field, vorticity field and pressure around the UUV under different depths and velocities are analyzed respectively. The results show that the existence of ice surface affects the resistance, lift, velocity field, vorticity field and pressure compared with free surface and infinite diving depth, which produces impact on the navigation of UUV, and the influence is related to diving depth and speed. The research provides a guidance for the safe navigation of UUV near the polar ice surface.

1. Introduction

Polar regions are important to scientific research, natural resources, and shipping. Most conventional polar scientific research and observation methods are based on scientific research ships and ice stations, and the fixed-point drilling method is usually used for underwater observation. With the development of unmanned underwater vehicle (UUV) technology, the introduction of high-tech intelligent equipment, such as underwater vehicles, can provide key technical support and great convenience to polar oceanography research. Most of the submarines currently used in polar scientific research are UUVs. Compared with conventional scientific research ships, ice stations, and other polar scientific research equipment, UUVs have the advantages of small size, good concealment, high autonomy, easy distribution, and recyclability. Furthermore, UUVs can operate under the ice for a long time, which significantly improves the efficiency of scientific research compared with the traditional method of drilling holes on ice. In addition, the application of UUVs in polar scientific research can greatly reduce the cost of scientific research, risk of investigators, and workload. UUVs are undoubtedly the most effective and promising technology for the comprehensive investigation of polar oceans on a large scale and for a long time.

During their operation, UUVs often face a wide range of ice distribution, which is necessary for sailing under the ice for a long time (see Fig. 1). The flow field around the vehicle sailing near the ice surface is hindered by the ice surface, making the hydrodynamic characteristics different from those of the free surface and infinite depth. The design of the hull type and attachment layout of the UUV in the polar area near ice also needs to consider the influence of ice on its hydrodynamic characteristics.

The REMUS UUV, which was developed by the United States in 1998, was mainly used to measure the underwater turbulence, salinity, and heat flow in the Arctic region. The National Marine Geographic Center of Southampton, UK, has developed the AUTOSUB series autonomous underwater vehicle (AUV) (McPhail and Pebody, 1997), which is mainly used for marine scientific research and military applications. AUTOSUB-II AUV was used to investigate the distribution of Antarctic krill in 2001 and 2005, and to observe the complex hydrological environment under the Fimbul ice. The Theseus AUV and Arctic Explore AUV designed by Canada successfully laid the polar optical cable and mapping under ice in 1996 and 2010, respectively. China also developed the Arctic ARV and Explore 1000 underwater robots, which have been successfully applied in polar scientific research.

Currently, there are limited studies on the hydrodynamic

* Corresponding author. School of Ocean Engineering and Technology, Sun Yat-sen University, Zhuhai, 519000, China.
** Corresponding author. School of Ocean Engineering and Technology, Sun Yat-sen University, Zhuhai, 519000, China.
E-mail addresses: jiangdp5@mail.sysu.edu.cn (D. Jiang), wutch7@mail.sysu.edu.cn (T. Wu).

https://doi.org/10.1016/j.oceaneng.2022.111304
Received 6 August 2021; Received in revised form 1 March 2022; Accepted 8 April 2022
Available online 21 April 2022

characteristics of UUVs under the interference of near ice surfaces. In most cases, the hydrodynamic characteristics of UUVs are studied under the condition of infinite depths or near free surfaces. The research methods of UUV hydrodynamic performance mainly include empirical formula estimation, model tests, and computational fluid dynamics (CFD) methods. Among them, the empirical formula cannot entirely consider the distribution of UUV appendages and interference between appendages, resulting in significant errors. Moreover, the model test is not suitable for the initial stage of UUV design because of its long cycle, high cost, and scale effect. Therefore, with the development of computer technology, the CFD method is widely used because of its low cost, high efficiency, and good reliability. Currently, the most effective and accurate research method combines CFD with the model test method. Sahin et al. (1997) first used the low-order panel method based on Green's theorem to predict the hydrodynamic characteristics of underwater vehicles. Ross et al. (2004) proposed a new method for measuring the longitudinal and transverse hydrodynamic coefficients of low-speed underwater vehicles based on the classical free decay test. Jagadeesh et al. (2009) studied the variation in the resistance, lift, and pitching moment coefficients of AUVs in different directions with the Reynolds number and angle of attack under the condition of a large depth in the towing tank. Mitra et al. (2019) and Lee et al. (2020) studied the hydrodynamic performance of underwater vehicles. In the research of underwater vehicle near surface navigation performance, Weinblum et al. (1950, 1951) conducted several near surface navigation model experiments to study the influence of geometric size, diving depth, and Froude number on submarine resistance. Hoerner (1965) continued Weinblum's research, and concluded that the wave resistance can be neglected when the depth exceeds five times its diameter. Subsequently, Vine et al. (1991), Mackay (2003), and Wilson-Haffenden et al. (2010) also conducted submarine near free surface navigation experiments. Alvarez et al. (2009) studied the wave resistance of AUVs with different shapes operating near the free surface, and calculated the wave resistance on the rotating body near the free surface using the first-order Rankine panel method to determine the hull type parameter with the least resistance. Polis et al. (2013) studied the influence of the free surface on the vertical hydrodynamic coefficients of the SUBOFF model using the CFD method, and tested the model in a towing tank. Mansoorzadeh and Javanmard (2014) studied the influence of the free surface on the AUV resistance coefficient. Shariati and Mousavizadegan (2017) calculated the SUBOFF model with and without appendages.

Thus far, there have been few studies on the hydrodynamic performance of UUV sailing near the ice surface. In this study, the CFD method was used to study the resistance coefficient, lift coefficient, velocity field distribution, and pressure distribution of the UUV under the influence of the free surface and ice under different sailing conditions.

The paper is organised as follows. Section 2 describes the numerical calculation method used. Section 3 describes the simulation model. Section 4 presents a verification of the simulation. Section 5 presents the results of the analysis. Section 6 describes the conclusions of this study.

2. Research model

In this study, the UUV Cormoran without appendages was selected as the research object. UUV Cormoran is a low-cost small ocean observation vehicle that was proposed by Alvarez et al. (2005), featuring the characteristics of autonomous surface vehicles and AUVs. In this study, the influence of rudder and wing appendages on the hydrodynamic characteristics of UUV Cormoran was not considered, and only the bare hull was selected to establish the geometric model. The parameters of the UUV Cormoran are listed in Table 1.

The coordinate system used in the calculation is shown in Fig. 2, using a right-handed coordinate system. Fig. 2-a and b depict the simulation and test models, respectively (Alvarez et al., 2009). The x-axis is parallel to the central axis of the UUV, and its positive direction is from the bow of the UUV to the stern. The positive direction of the z-axis is vertically upward, and z = 0 is at the free surface.

3. Numerical simulations

3.1. Numerical simulation method

The software used in this research is STAR CCM+. The finite volume method is used as the discrete method. The motion of incompressible Newtonian fluid satisfies the time-dependent conservation of mass and three-dependent conservation of momentum equations, which can be expressed as (Wang et al., 2021):

$$\frac{\partial}{\partial t}\int_{CV}\rho\varphi dV+\oint_{A}\boldsymbol{n}\cdot(\rho\varphi\boldsymbol{u})dA=\oint_{A}\boldsymbol{n}\cdot(\Gamma_{\varphi}\nabla\varphi)dA+\int_{CV}S_{\varphi}dV \tag{1}$$

where CV is the three-dimensional control volume over which the volumetric integration is performed. A is the boundary surface of the control volume. φ is the rate of change of property. $\boldsymbol{n}$ is the unit vector, $\boldsymbol{u}$ represents the instantaneous velocity vector, ρ is the fluid density, and Γ_{φ} is the diffusion coefficient.

The SST (Shear Stress Transfer) k-ω improved delayed detached eddy simulation (IDDES) was selected for the turbulence model to capture the

Table 1
UUV Cormoran parameters.

UUV Cormoran	
Scale	1:1
Diameter (m)	0.16
Total length (m)	1.42
Wet surface (m^2)	0.63
Volume (m^3)	0.0245

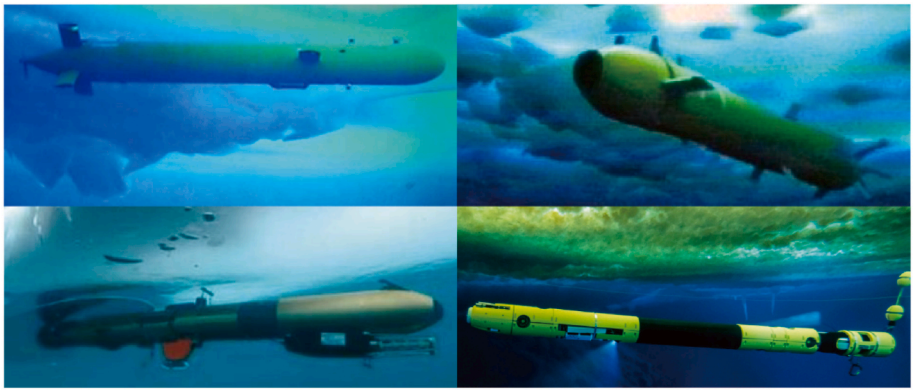

Fig. 1. AUV sailing near ice surface.

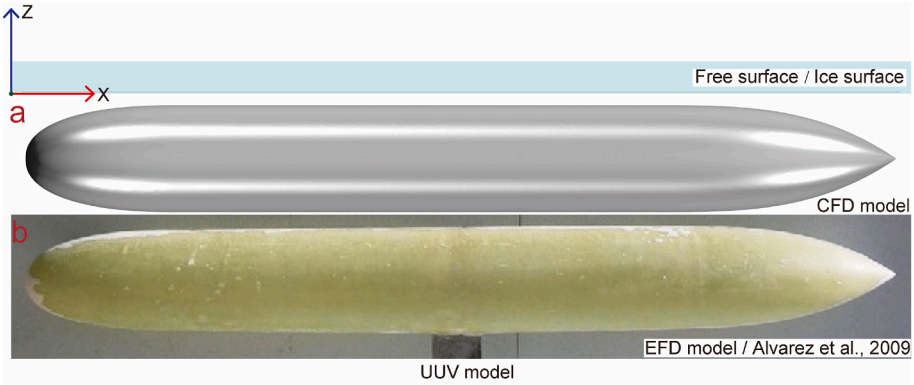

Fig. 2. UUV model and coordinate system.

vortex structure of the flow field around the UUV, particularly the flow field near the stern area (Menter, 1994). The switch of the traditional detached eddy simulation (DES) and delayed detached eddy simulation (DDES) method from RANS to LES location is based on the local grid refinement, which usually leads to an error called a log-layer mismatch. The IDDES was recommended to mitigate these problems (Spalart, 2009; Sharma et al., 2019). By combining the functions of the Reynolds-averaged Navier–Stokes (RANS) model in the boundary layer and the large eddy simulation (LES) model in the unsteady separation region, the SST k-ω IDDES unites the advantages of the SST k–ω RANS and LES. The number of grids and calculation amount can be reduced using the RANS method in the near wall area, and the LES method is used in the area far away from the wall to ensure that the large-scale separated flow can be accurately captured. The free surface above the UUV was modelled using the two-phase volume-of-fluid (VOF) technique (Hirt and Nichols, 1981) with the high-resolution interface capturing (HRIC) scheme (Muzaferija, S, 1998).

3.2. Computational domain and boundary conditions

As shown in Fig. 3, only half of the UUV was selected for the calculation under different conditions. As the UUV Cormoran 3D model selected in this study is symmetrical about the mid-longitudinal section of the hull, only half of the UUV can be selected to reduce the amount of calculation. The calculation domain UUV sailing near an infinite depth is shown in Fig. 3-a. The length, width, and height of the calculation domain are 3.75 L, L, and 3 L, respectively, where L is the length of the UUV hull. Then, it is 0.75 L at the front of the hull, L at the side of the hull, 1.5 L below the top, and 2 L at the rear of the hull. The calculation domain UUV sailing near the free surface is shown in Fig. 3-b. The length, width, and height of the calculation domain are 3.75 L, L, and 1.75 L. Thus, it is 0.75 L at the front of the hull; L at the side of the hull; 0.75 L and L at the top and bottom of the free surface, respectively; and 2 L at the rear of the hull. The calculation domain UUV sailing near the ice surface is shown in Fig. 3-c. The length, width, and height of the calculation domain are 3.75 L, L, and L. Hence, it is 0.75 L at the front of the hull, L at the side of the hull, L below the ice surface, and 2 L at the rear of the hull.

The boundary conditions for different conditions are shown in Table 2.

3.3. Meshing sensitivity study and results verification

In this study, the UUV Cormoran geometric model is sharp around the bow and stern. Moreover, the mesh generation method should be able to accurately describe the shape of the UUV bow and stern to ensure mesh quality. Additionally, it is necessary to accurately capture the wave generated by the free surface as well as the force and vortex structure around the hull surface and ice surface in the calculation of UUV hydrodynamic characteristics. Therefore, trim meshes of STAR-CCM + are used to describe the computational domain, and some important areas which influence the calculation results were refined. Furthermore, for the UUV hull surface, ice surface, and other near wall boundary layer regions, a prism layer mesh was used. The numerical calculation of the total resistance coefficient Ct under the conditions of 0.1 m depth and 1.062 m/s speed is selected to verify the mesh sensitivity. By adjusting the base size set during mesh division, three sets of meshes with different densities are generated, namely coarse mesh,

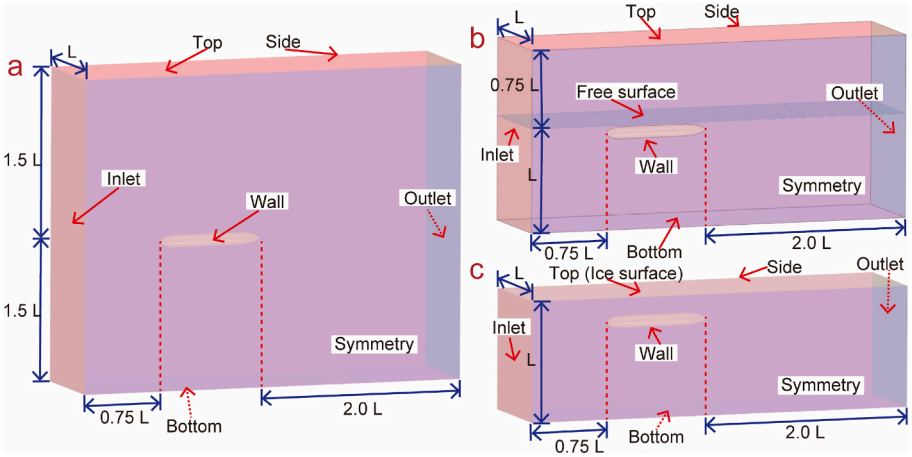

Fig. 3. Computational domain for different conditions.

Table 2
Boundary conditions for different conditions.

Boundary name	Boundary conditions		
	Infinite depth	Near free surface	Near ice surface
Inlet/ Bottom/ Top/Side	Velocity inlet, velocity based on flat VOF wave, along the x-direction	Velocity inlet, velocity based on flat VOF wave, along the x-direction	Velocity inlet, velocity based on flat VOF wave, along the x-direction
Outlet	Pressure outlet, based on flat VOF wave hydrodynamic pressure	Pressure outlet, based on flat VOF wave hydrodynamic pressure	Pressure outlet, based on flat VOF wave hydrodynamic pressure
Wall	No slip, impenetrable and fixed wall	No slip, impenetrable and fixed wall	No slip, impenetrable and fixed wall
Top	/	/	No slip, impenetrable wall with x-direction velocity (ice surface)
Symmetry	Plane of symmetry	Plane of symmetry	Plane of symmetry

medium mesh and fine mesh, and the total number of coarse, medium and fine meshes is 2.303, 3.902 and 6.950 million, respectively. Roy et al. (2007) presented methods for assessing the uniformity of the mesh refinement with Cartesian grid, and the mesh refinement ratio r_G was considered as follows:

$$r_G = \left(\frac{N_{fine}}{N_{coarse}}\right)^{1/d} \tag{2}$$

where the total number of meshes is noted as N, d is the dimensionality of the computing problem and its value in the present study is 3. The mesh refinement factor for the fine/medium and medium/coarse meshes is 1.21 and 1.19, respectively. The mesh refinement ratio of fine to medium (medium to coarse) grids is approximately 1.2, which is consistent with references (Roy et al., 2007; Guo et al., 2017; Huang et al., 2021). The numerical calculation results of the total resistance coefficient C_t under different meshes are compared with the experimental results obtained by (Alvarez et al., 2009). The experimental Ct is 0.00989. The comparison result is shown in Table 3. The calculated results under three different dense meshes are consistent with the experimental values, and the errors are all within 5%.

In order to verify the accuracy of the calculation method in this study, three groups of total resistance coefficient Ct are verified on the basis of fine mesh calculation. In 2009, Alvarez et al. (2009) conducted an experiment with a free surface using the UUV Cormoran model with a scale ratio of 2:1. Three groups of experimental resistance coefficient (Ct) values were selected for comparison with the simulation results, as shown in Table 4. When the diving depth is 0.1 m, the velocities are 0.916, 1.062 and 1.195 m/s; the error between the numerical results of the resistance coefficient (Ct) obtained using this method and the experimental results are within 5%, which correlates with the experimental value. Thus, it can be proved that the numerical model and method used in this study are accurate.

The velocity field distribution and waveforms under three density meshes are shown in Figs. 4 and 5. It can be seen that the velocity field distribution and waveforms under the three conditions have little difference. After the wake region is locally enlarged, it can be found that the fine mesh can capture flow field changes finer than the coarse mesh and the medium mesh. In theory, the medium mesh can reduce the computational cost considerably and still achieve a tolerable level of numerical accuracy of resistance, lift coefficient and finer flow field. By comparison and analysis, the computing resources can meet the needs of finer meshes. In order to obtain finer computing results, all the calculations in this study are carried out in fine meshes.

Table 3
Comparison of Ct.

Number of meshes	Ct	Error
Coarse	0.00952	3.66%
Medium	0.00991	0.28%
Fine	0.01022	3.42%
EFD	0.00989	–

Table 4
Resistance coefficient Ct.

Velocity (m/s)	Resistance coefficient (Ct)		Error
	Experimental results	Numerical results	
0.916	0.00913	0.009229	1.08%
1.062	0.00989	0.009918	3.42%
1.195	0.01291	0.012274	−4.93%

The computational mesh of the UUV under different conditions are shown in Fig. 6, and Fig. 6-a,b and c are the overall meshes with local mesh refinement of wake, free/ice surface of the computational domain under different conditions, Fig. 6-e is the Kelvin refinement of the free surface, Fig. 6-d and f are the meshes around the hull and boundary layer mesh.

4. Results

4.1. Resistance coefficient

Fig. 7 shows the relationship of the resistance coefficient (Ct) with Froude number (Fr) when the diving depth is 0.1 m at the near free surface, near ice surface, and infinite depth. In the calculation, the UUV velocities were 0.5144, 1.195, 1.5432, 2.0576 and 2.572 m/s, and the corresponding Fr values were 0.138, 0.32, 0.458, 0.552 and 0.763, respectively. Fig. 7 demonstrates that, when the diving depth is 0.1 m, the resistance coefficient first increases, then decreases, and subsequently, increases with the increase in Fr. Under the condition of infinite depth, the resistance coefficient of UUV Cormoran decreases with an increase in velocity, and tends to stabilise. Compared with the near free surface condition, the resistance coefficient decreases significantly when it sails near the ice surface. With the increase in velocity, Ct exhibits a downward trend, and finally, tends to stabilise.

Fig. 8 shows the resistance coefficient for different diving depths near the free surface and near the ice surface when the velocity was 1.195 m/s (Fr = 0.32). When the diving depth of the UUV Cormoran changes from D to 5D (where D is the diameter of the UUV), the resistance coefficient (Ct) decreases as the diving depth increases, and finally, tends to become similar to the value of the infinite diving depth condition at the same velocity. With the increase in the diving depth, the difference in Ct between the near free surface and near ice surface conditions also decreases gradually. When the diving depth is equal to 3D and 5D, the difference is extremely small, almost equal, and equal to the resistance coefficient of infinite depth at the same velocity. Therefore, the influence of the ice surface and free surface on the resistance coefficient of the UUV can be ignored when the diving depth is more than three times the diameter (3D).

4.2. Lift coefficient

Fig. 9 shows the relationship of the lift coefficient (Cl) with the Froude number (Fr) when the diving depth is 0.1 m at the near free surface, near ice surface, and infinite depth. As shown in Fig. 8, the lift without buoyancy is almost zero for UUVs at infinite depth. Under the condition of near the free surface, the lift coefficient (Cl) of UUV Cormoran decreases sharply with the increase in ship velocity; moreover, a negative lift even appears when Fr = 0.458 and 0.763. This is because, as the velocity increases, the wave resistance increases, which produces

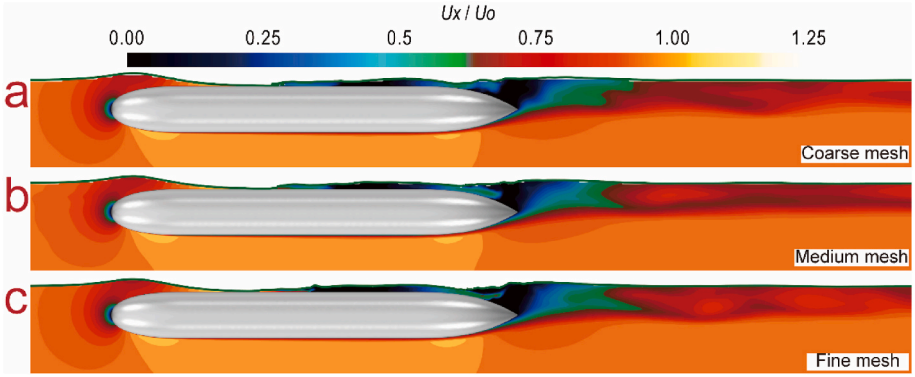

Fig. 4. The velocity field distribution under three density meshes.

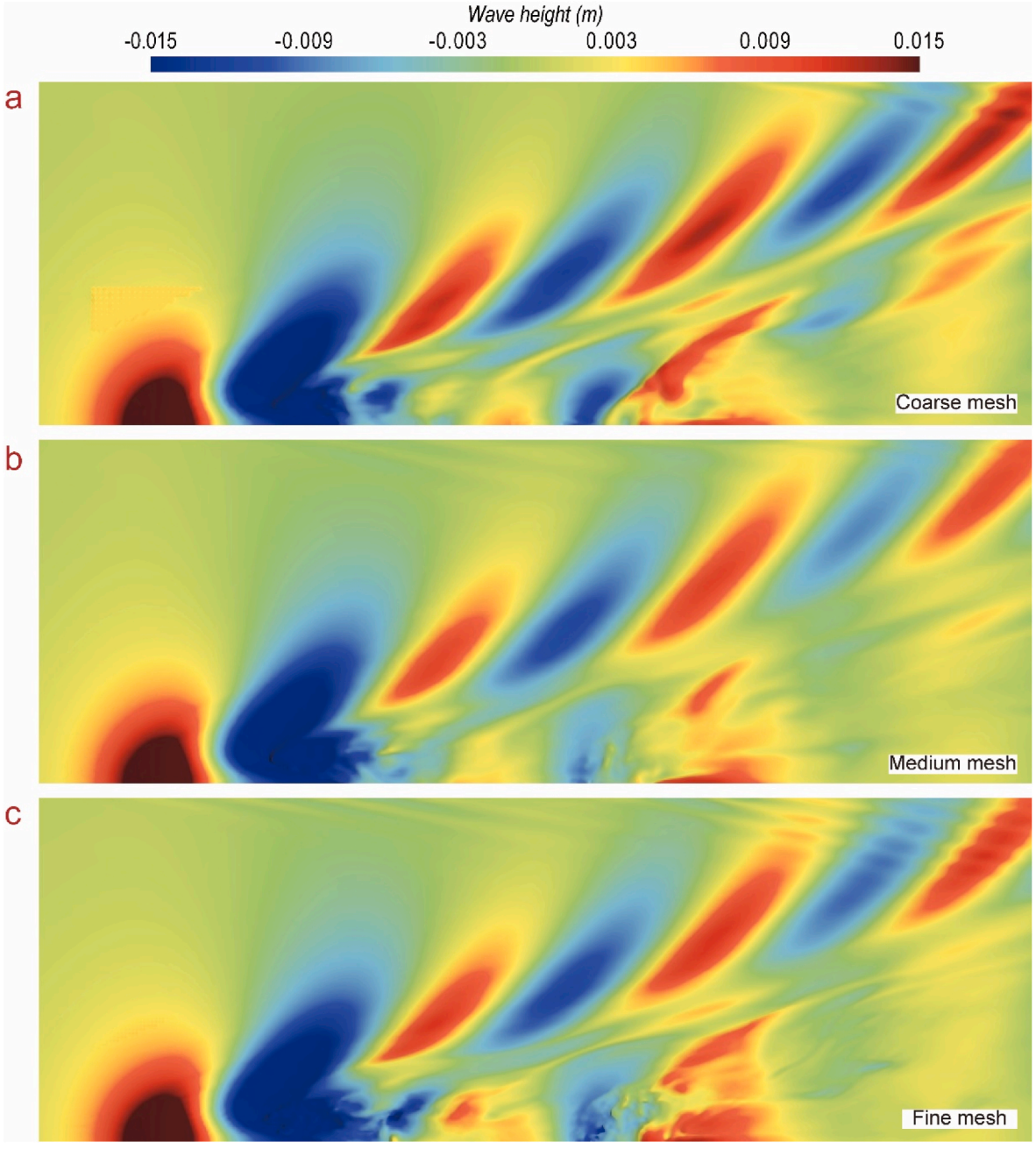

Fig. 5. The waveforms under three density meshes.

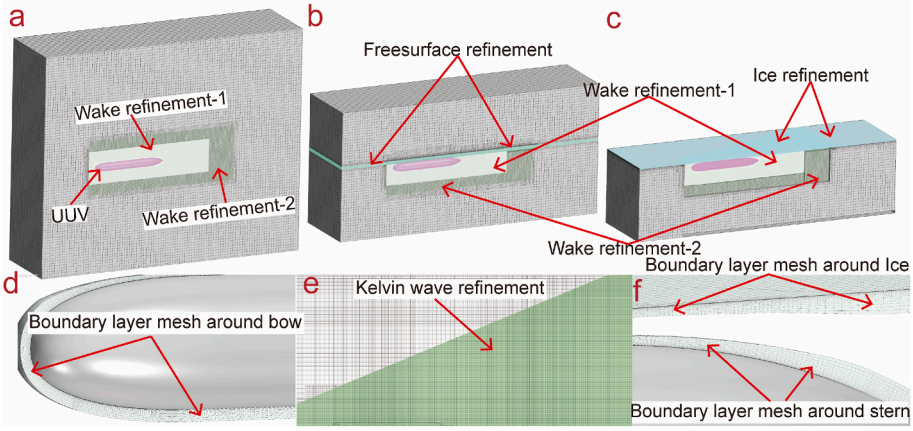

Fig. 6. Mesh refinement for different conditions.

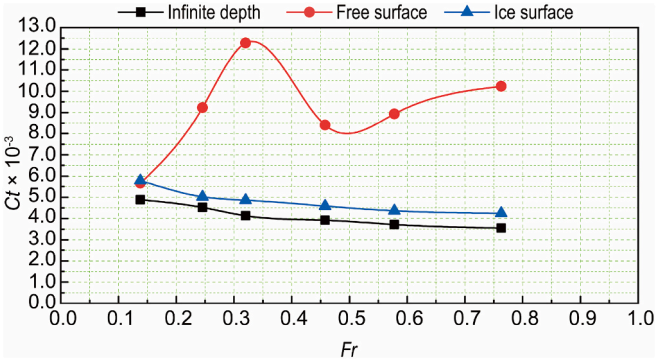

Fig. 7. Resistance coefficient (*Ct*) with different *Fr*.

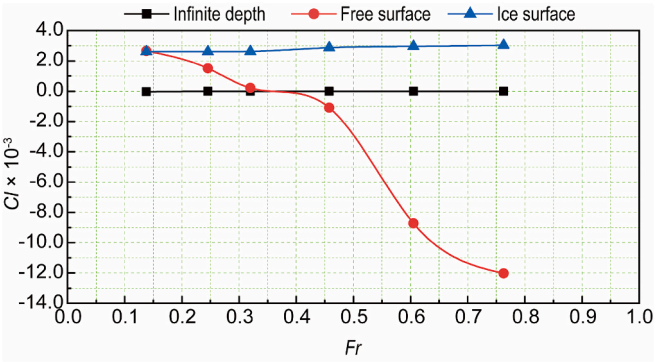

Fig. 9. Lift coefficient (*Cl*) with different *Fr*.

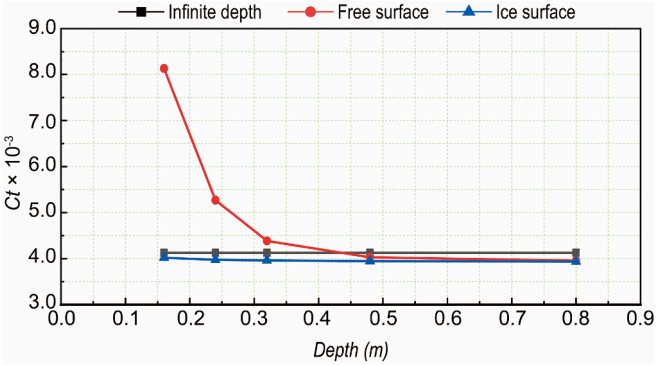

Fig. 8. Resistance coefficient (*Ct*) with different diving depths.

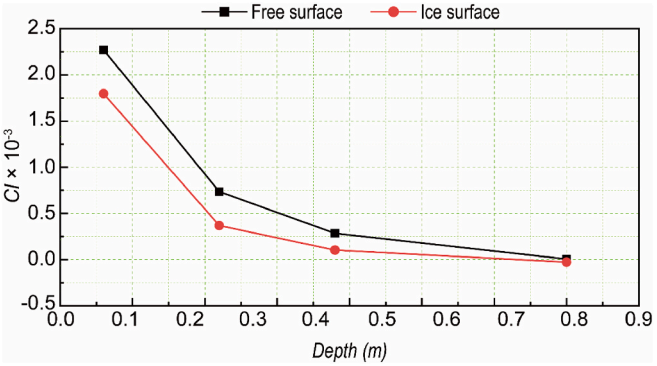

Fig. 10. Lift coefficient (*Cl*) with different diving depth.

downward pressure on the hull, resulting in a negative lift. The lift of the UUV near the ice surface is considerably greater than that near the free surface and infinite depth, indicating that the ice surface has an evident upward suction effect on the UUV. As the velocity increases, *Cl* near the ice surface increases slightly, and eventually, tended to stabilise.

Fig. 10 shows the lift coefficient with different diving depths near the free surface and near the ice surface when the velocity is 1.195 m/s (*Fr* = 0.32). Fig. 10 shows that the lift coefficient (*Cl*) of the UUV Cormoran near the free surface gradually decreases with the increase in diving depth, and finally, tends to stabilise at an infinite diving depth of zero. Compared with the condition of the near free surface, the lift force of the UUV on the near ice surface is less than that at the corresponding depth of the near free surface. When the diving depth increases from D to 5D, the lift coefficient (*Cl*) gradually decreases near the ice surface, and finally, tends to stabilise at an infinite diving depth of zero.

4.3. Velocity

Fig. 11 shows the velocity field distribution under different conditions at a velocity of 0.5144 m/s. Fig. 11a shows the velocity field distribution at infinite depth. Fig. 11b shows the velocity field distribution at the free surface with a depth of 0.1 m. Fig. 11c shows the velocity field distribution near the ice surface at a depth of 0.1 m. The x-axis velocity (U_x) is dimensionless to obtain U_x/U_0, and U_0 represents the initial navigation velocity of the UUV. The velocity field around the ship is symmetrical at an infinite depth condition. When sailing near the ice surface, the velocity fields of the bow (label head) and stern are asymmetrically distributed, owing to the influence of the ice surface, and the

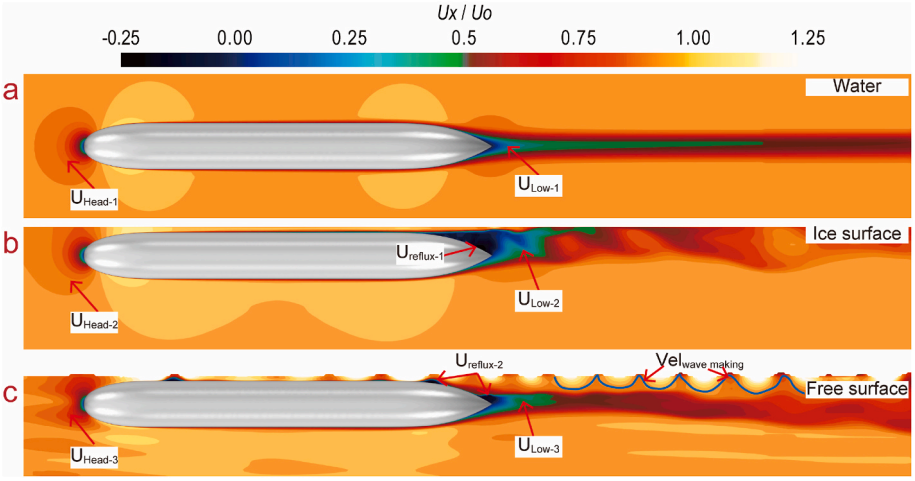

Fig. 11. Dimensionless velocity field of (a) infinite depth, (b) ice surface, and (c) free surface at 0.1 m depth.

negative velocity (label $U_{reflux\text{-}1}$) appears at the stern position. Moreover, owing to the adsorption effect of the wall, the low-velocity region (label $U_{LOW\text{-}2}$) of the stern region is larger than the infinite diving depth (label $U_{LOW\text{-}1}$), and it is distributed above the stern of the hull. In the near free surface condition, the asymmetry of the velocity distribution is weaker than that of the ice surface but stronger than that of the infinite depth. The free surface is disturbed by the hull, and the velocity distribution of the hull is affected by the free surface. The negative velocity (label $U_{reflux\text{-}2}$) and low-velocity region (label $U_{LOW\text{-}3}$) also appear in the stern area. Influenced by the free surface, a new wave-making region formed

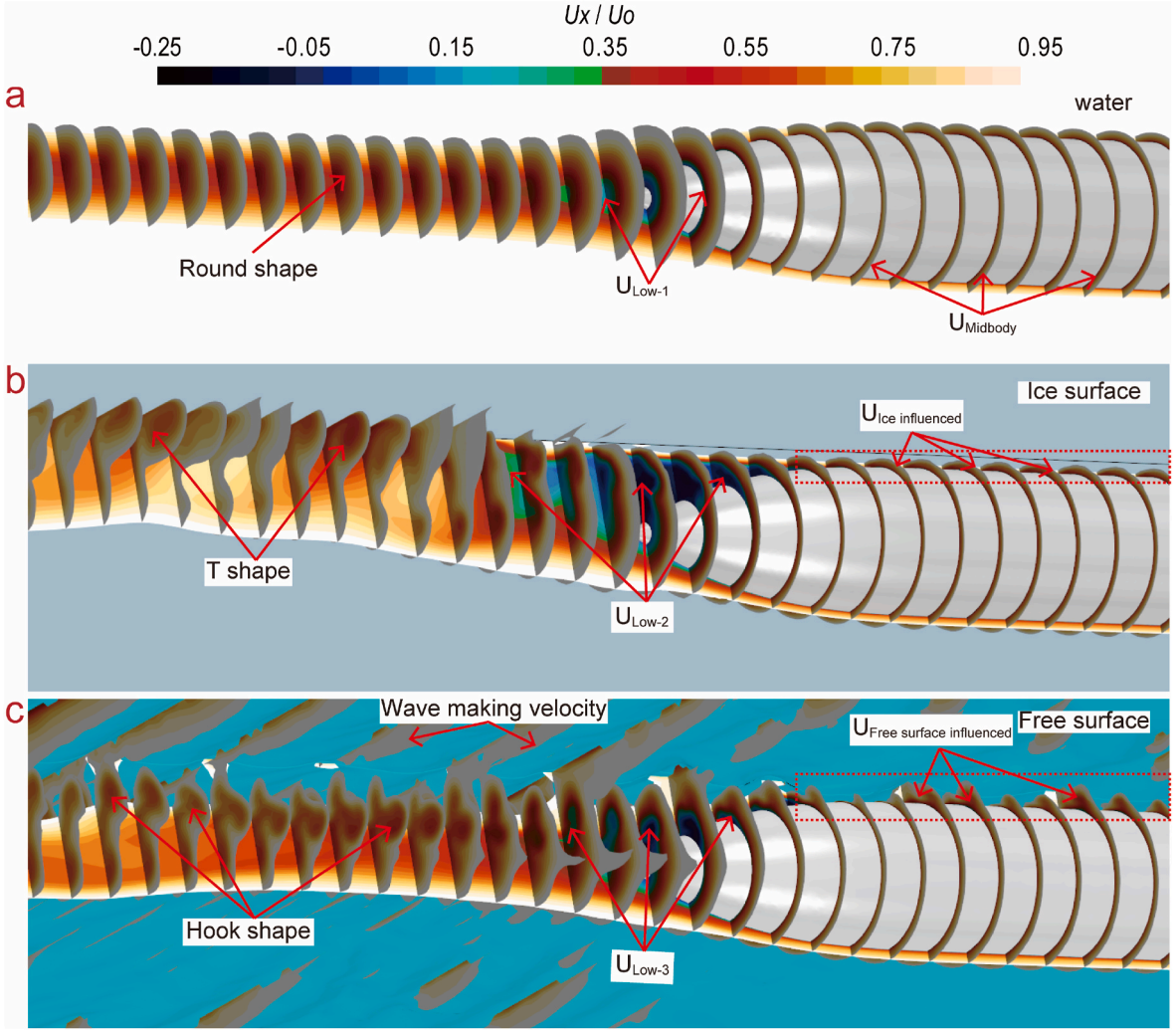

Fig. 12. Dimensionless velocity field of the stern area with different planes along longitudinal direction: (a) Infinite depth; (b) Ice surface; and (c) Free surface.

in the wake area, and the new wave-making velocity distribution shape has the synchronous phase of transverse wave system with the free surface.

Fig. 12 shows the boundary layer field of the stern area with different planes along the longitudinal direction at a velocity of 0.5144 m/s. Fig. 10a, b, and 10c, respectively, show the velocity fields of the stern area at infinite depth, near the ice surface at a depth of 0.1 m, and at the free surface with a depth of 0.1 m. The boundary layer field was defined as $U_x/U_0 < 0.95$. The distribution of flow field in different sections of the stern area is symmetrical under the condition of infinite depth, and the shape of the velocity distribution of the wake region is approximately circular (label round sharp). Under the condition of near ice and free surface, the velocity field distribution of different sections changes under the near ice and free surface conditions, and the low-velocity region appears in several sections near the stern region. Additionally, the low-velocity region (label $U_{low\text{-}2}$) under the near ice conditions exceeds that (label $U_{low\text{-}3}$) near the free surface, and the low-velocity zone decreases with the distance from the stern. The shape of the velocity distribution of the wake region under the near ice conditions is an approximate T-shaped distribution (label T sharp). The shape of the velocity distribution of the wake region under the near free surface condition is a similar hook-shaped distribution (label hook sharp). Under the near ice surface condition, the roundness of the circular velocity distribution ($U_{midbody}$) above the UUV is weakened by ice interference (label $Vel_{ice\ influenced}$). Under the near free surface condition, a velocity distribution is influenced by the free surface above the UUV which has the synchronous phase of transverse wave system with the free surface (label $Vel_{freesurface\ influenced}$). Moreover, there is a UUV wave-making velocity distribution in the free surface region (label $Vel_{wavemaking}$).

Fig. 13 shows the dimensionless velocity field distribution at different velocities for a diving depth of 0.1 m. Among them, Fig. 13-a, b, c, and d show the dimensionless velocity field distributions when the velocities are 0.5144, 1.195, 1.5432, and 2.5722 m/s, respectively. A low-speed zone is formed behind the stern, owing to the influence of the ice surface, and a negative velocity (label U_{reflux}) appears at the stern area. The range of the stern reflux area was $U_{reflux\text{-}4} > U_{reflux}\text{-}3 > U_{reflux\text{-}2} > U_{reflux\text{-}1}$. The area of the low-speed zone decreases and gradually increases; however, the asymmetry of the velocity field gradually increases, indicating that the suction effect of the ice surface increases with the increase in velocity.

Fig. 14 shows the dimensionless velocity field distribution under different diving depths near the ice surface when the velocity is 1.195 m. Fig. 14a, b, c, d, e, and f show the velocity field distribution when the diving depths are 0.625D, D, 2D, 3D, 5D, and infinite depth, respectively. When the diving depth is 0.625D and D, the flow field distribution around the bow and stern is asymmetric, owing to the influence of the ice surface, and there is a reflux zone (label $U_{reflux\text{-}1}$ and $U_{reflux\text{-}2}$) behind the stern. When the diving depth is greater than 2D, the trend of the asymmetric flow field is weaker than that of 0.625D and D, and the flow field in the front of the bow (label head) tends to be symmetric. With the increase in diving depth, the influence of the ice surface effect on the velocity distribution around the UUV decreases gradually.

When the diving depth exceeds 2D, the reflux region of the stern area disappears, and the symmetrical velocity distribution of the bimodal shape (label midbody) at the middle body of the UUV is gradually restored; the influence of the ice surface on the velocity distribution at the middle body can be ignored when the depth is 3D. The velocity distribution in the wake area is significantly affected by the diving depth. The axial and spanwise distribution ranges of low velocity in the wake area gradually decrease with increasing diving depth. When the depth is greater than 3D, the wake velocity distribution is the same as that at an infinite depth. Moreover, the adsorption effect of the free surface wake is weakened, and the oblique flow angle in the low-speed region gradually decreases, as illustrated by Figs. 19 and 22. Fig. 15 is the velocity distribution curve along the X direction of UUV. It can be seen that the velocity distribution around the UUV hull under different diving depths is roughly the same. In the wake area, the velocity distribution under different diving depths shows the difference and the change regularities are consistent with Fig. 14.

4.4. Line integral convolution around UUV

Line integral convolution (LIC) is a technique proposed by Cabral and Leedom (1993) to visualise a vector field. Compared to other integration-based techniques that compute the field lines of the input vector field, LIC is capable of displaying all structural features of the vector field, without the need to adapt the start and end points of the

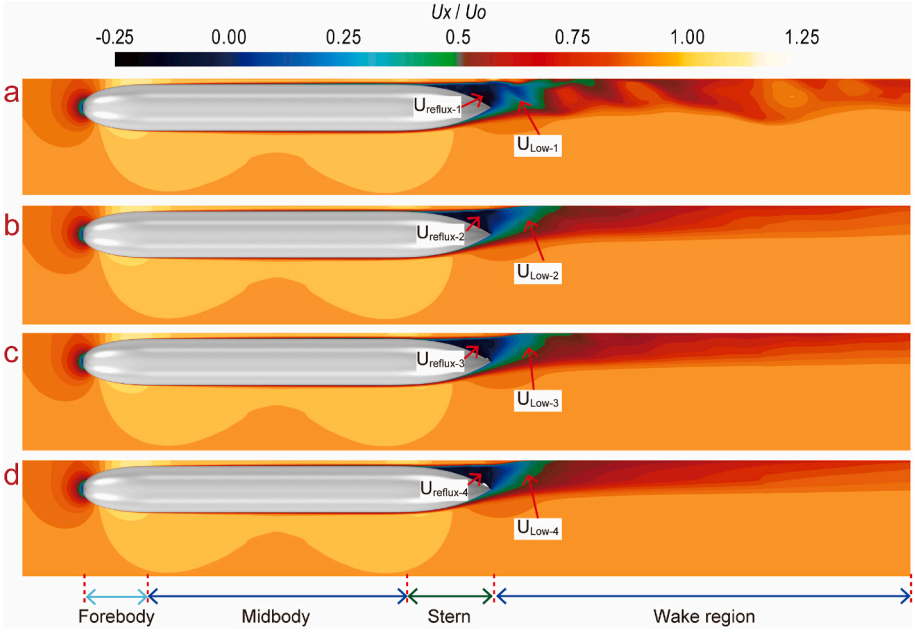

Fig. 13. Dimensionless velocity field distribution at different velocities near the ice surface: (a) V = 0.5144 m/s; (b) V = 1.195 m/s; (c) V = 1.5432 m/s; and (d) V = 2.5722 m/s.

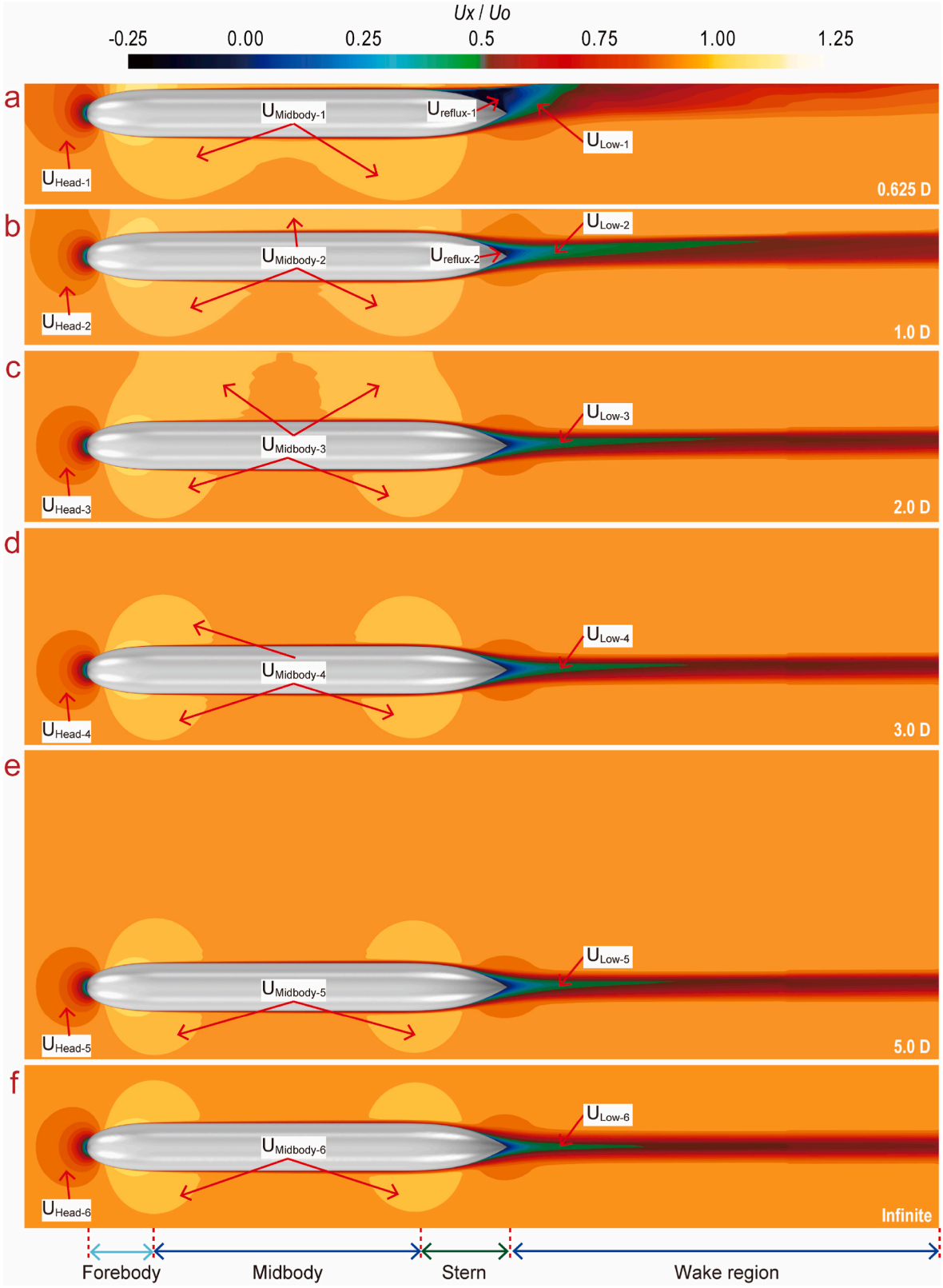

Fig. 14. Distribution of dimensionless velocity field under different diving depths near the ice surface: (a) 0.625D; (b) D; (c) 2D; (d) 3D; (e) 5D; and (f) Infinite depth.

field lines to the specific vector field. The saddle, foci, Centre, node points and pure shear are important characteristics for marking fluid properties. The flow characteristics in LIC are analyzed in this section based on these characteristic points. Perry and Chong (1987) and Smits and Lim (2012) described the physical meanings and definitions of saddle, foci, center, node and pure shear in detail, and gave the schematic cases. Fig. 16 shows the LIC around the UUV in the middle longitudinal plane coloured with turbulent kinetic energy (TKE) under different conditions with a velocity of 0.5144 m/s. Fig. 16-a, b, and c show the conditions of infinite depth, near ice surface, and near the free

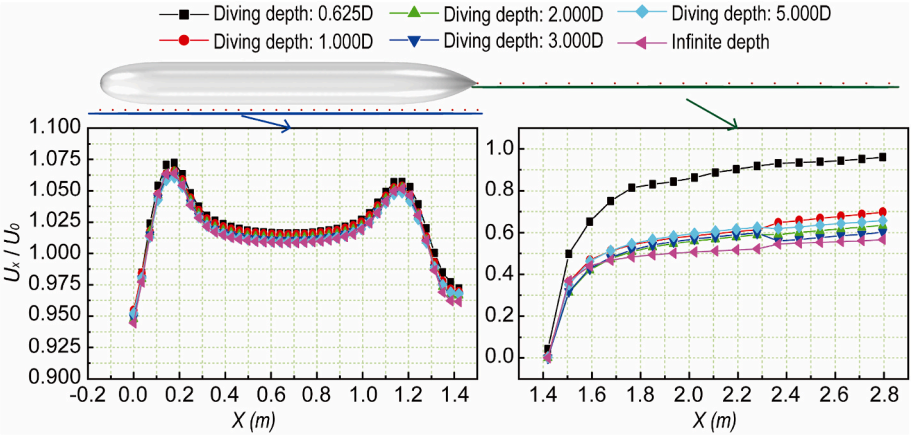

Fig. 15. Velocity distribution curve along the X direction of UUV.

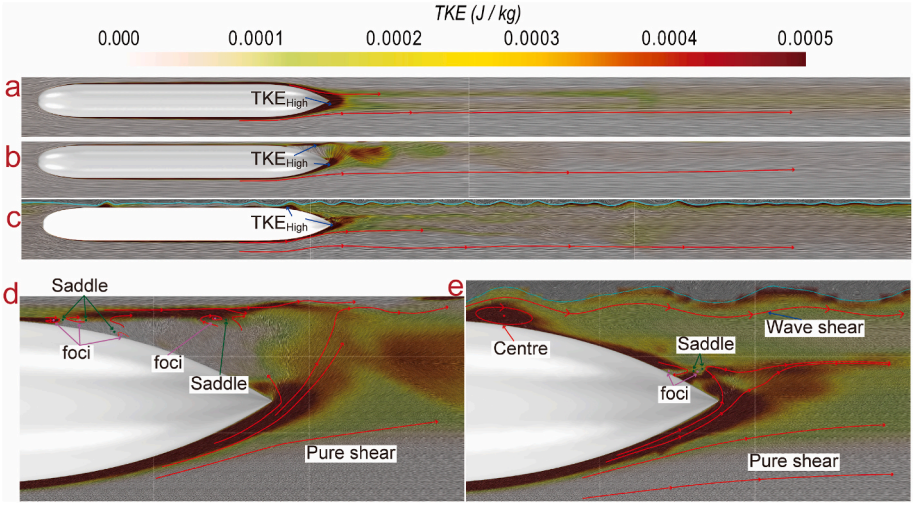

Fig. 16. LIC around UUV in middle longitudinal plane coloured with TKE under the conditions of (a) infinite depth, (b) near ice surface, and (c) near free surface. Enlarged views of the stern region of UUV under (d) near ice surface and (e) free surface conditions.

surface, respectively. Fig. 16-d and e are enlarged views of the stern region of the UUV near the ice surface and free surfaces, respectively. At an infinite depth, the LIC streamline in the wake region and high TKE region are symmetrically distributed along the UUV axis. Under the conditions of near ice surface and free surface, the flow characteristics of UUV are significantly different from those at infinite water depth. As shown in Fig. 16b, the wall effect of the ice sheet makes the LIC distribution of the UUV asymmetric, and the LIC has apparent oblique flow and reflux characteristics in the wake area. Further, a high TKE presents an asymmetric and upward distribution. In Fig. 16-d, the local enlarged view of the characteristics of wake reflux and oblique flow shows that the reflux area contains multiple saddle and foci points. In Fig. 16-c, the distribution of the LIC and TKE of the UUV under the effect of the free surface is also asymmetric. Compared with those under the ice surface condition, the oblique flow and reflux characteristics of the LIC in the wake area are relatively weak. The streamline outside the TKE region is similar to the pure shear flow. The interaction between the free surface and UUV forms a wave shear-influenced LIC distribution. In Fig. 16-e,

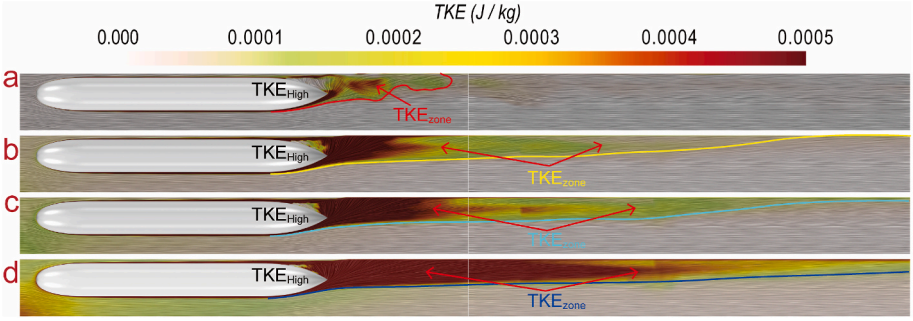

Fig. 17. LIC around UUV in the middle longitudinal plane coloured with TKE at different velocities near the ice surface: (a) V = 0.5144 m/s; (b) V = 1.195 m/s; (c) V = 1.5432 m/s; and (d) V = 2.5722 m/s.

the enlarged view of the characteristics of wake reflux and oblique flow shows that the wake area contains one centre and multiple saddle and foci points.

Fig. 17 shows the LIC around the UUV in the middle longitudinal plane coloured with TKE with different velocities. Fig. 17-a, b, c, and d show velocities of 0.5144, 1.195, 1.5432, and 2.5722 m/s, respectively. The diving depth is 0.1 m (0.625D). With the increase in velocity, the range of high TKE in the UUV wake area increases, and LIC appears. The flow is enhanced by the wall effect of the ice surface, and has significant oblique flow characteristics pointing to the ice surface.

Fig. 18 is the enlarged view of LIC around UUV in the middle longitudinal plane coloured with TKE at different velocity near ice surface. Fig. 18-a, b, c, and d show velocities of 0.5144, 1.195, 1.5432, and 2.5722 m/s, respectively. In Fig. 15, the local enlarged view of the wake reflux and oblique flow characteristics shows that the reflux area contains multiple saddle and foci, unstable foci, and centre points. As the velocity increases from 0.5144 m/s to 2.572 m/s, the adsorption effect of the ice surface on the wake increases, and the angle of the oblique flow increases. Additionally, with the increase in velocity, the amplitude and range of TKE in the UUV wake region increase; the streamline outside the high TKE region is rarely affected by the ice surface and velocity, showing similar pure shear flow characteristics.

Fig. 19 shows the LIC around the UUV in the middle longitudinal plane coloured with TKE at different diving depths near the ice surface with a velocity of 1.195 m/s. Fig. 19-a, b, c, d, and e show diving depths of 0.625D, D, 2D, 3D, and 5D, respectively. With the increase in the diving depth, the influence of the wall effect on the flow field around the UUV gradually decreases, showing that the distribution of TKE gradually becomes symmetrical, and the degree of oblique flow of the wake gradually decreases. Additionally, the enlarged view demonstrates that, with the increase in the diving depth, the TKE of the wake gradually weakens, showing that the number of saddle and foci points reflecting the flow field gradually decreases.

4.5. Vortical structures

The three-dimensional visualisation of vortical structures can be expressed by the Q-criterion, which defines a vortex by the region where the rate of rotation tensor (Ω_{ij}) exceeds the strain rate tensor (S_{ij}) (Liu et al., 2019; Zhao et al., 2021; Cao et al., 2021). $Q = \frac{1}{2}(|\Omega|^2 - |S|^2)$, $\Omega_{ij} = \frac{1}{2}\left(\frac{\partial u_i}{\partial x_j} - \frac{\partial u_j}{\partial x_i}\right)$,and $S_{ij} = \frac{1}{2}\left(\frac{\partial u_i}{\partial x_j} + \frac{\partial u_j}{\partial x_i}\right)$. Fig. 20 shows the vortical structures expressed by the Q-criterion at $Q = 0.5$, around the UUV coloured with dimensionless velocity U_x/U_0 under different conditions with a velocity of 0.5144 m/s. Fig. 20-a, b, and c show the conditions of infinite depth, near the ice surface, and near the free surface, respectively.

Fig. 20 shows that the wall effect of the ice surface and the influence of the free surface have a significant effect on the three-dimensional vortex structure of the UUV. In the bow area, the bound vortex structures under these three conditions are extremely similar; the difference is that there is a vortex (label vortex) on the ice surface in the near ice condition. For the middle body region of the UUV, the bound vortex structures under the three conditions are significantly different. Under the condition of infinite depth, the bound vortex in the middle body of the UUV is a strip-shaped distribution (label Vor_{body}). Although the bound vortex in the near ice surface condition is also distributed in the strips, the strips are narrower and denser. For the near free surface condition, in addition to the strip-shaped distribution of the bound vortex in the middle body section, which is similar to the infinite depth, there is also a free surface-influenced vortex which has the synchronous phase of transverse wave system with the free surface in the upper part of the UUV ($Vor_{freesurface}$). In the stern region of the UUV, the shape of the bound vortex is similar; however, the boundary is different (green, yellow, and blue dotted lines). The ice-surface influenced vortex structure is produced in the upper part of the UUV stern area ($Vor_{ice\ influenced}$). Moreover, the stern low-speed region is $U_{low\text{-}3} > U_{low\text{-}2} > U_{low\text{-}1}$. In the wake area, the wake vortices under the three conditions were significantly different. With a UUV velocity of 0.5144 m/s, the wake vortex range of the UUV is small, and the vortex system propagation is stable under the condition of infinite depth. In the near ice surface condition, the shedding wake vortex of the UUV interacts with the ice surface, showing a hairpin vortex attached along the ice surface (Vor_{wake} and $Vor_{Hairpin}$), and the development range of the wake vortex was the longest under the same vortex structure criterion coefficient. For the near free surface condition, the wave-making vortex system corresponding to Kelvin wave making was formed after the free surface interacted with the UUV ($Vor_{wavemaking}$). The wake vortex range corresponding to that of the near ice surface condition is slightly smaller.

Fig. 21 shows vortical structures around UUVs coloured with dimensionless velocity U_x/U_0 at different velocities near the ice surface. Fig. 21a, b, c, and d show velocities of 0.5144, 1.195, 1.5432, and 2.5722 m/s, respectively. The diving depth is 0.625D. Fig. 22 is the close-up of Fig. 21.

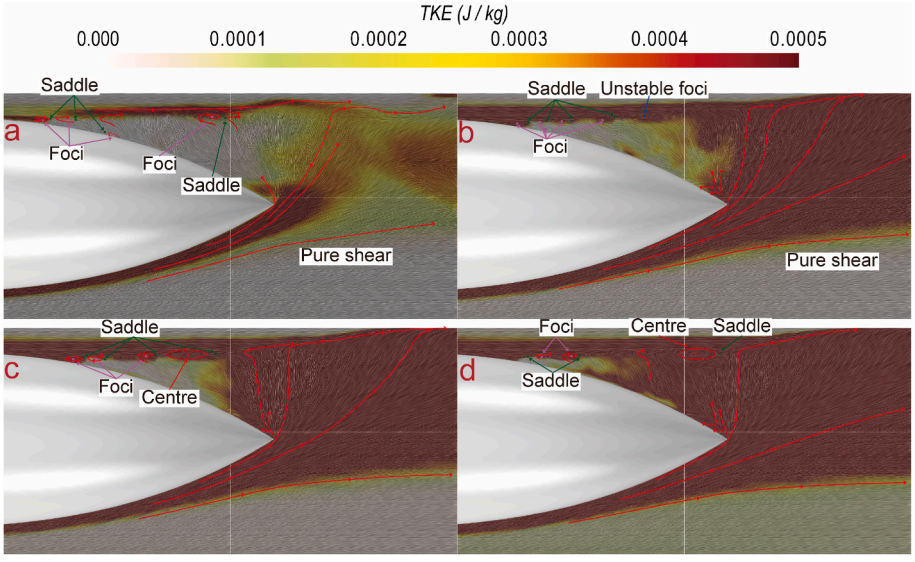

Fig. 18. Enlarged view of LIC around UUV in middle longitudinal plane coloured with TKE at different velocities near the ice surface: (a) V = 0.5144 m/s; (b) V = 1.195 m/s; (c) V = 1.5432 m/s; and (d) V = 2.5722 m/s.

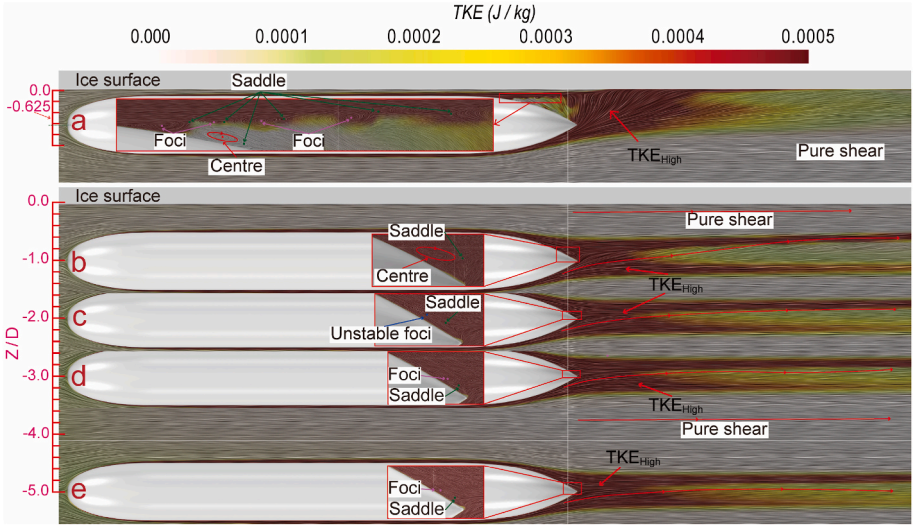

Fig. 19. LIC around UUV in the middle longitudinal plane coloured with TKE at different diving depths near the ice surface: (a) 0.625D; (b) D; (c) 2D; (d) 3D; and (e) 5D.

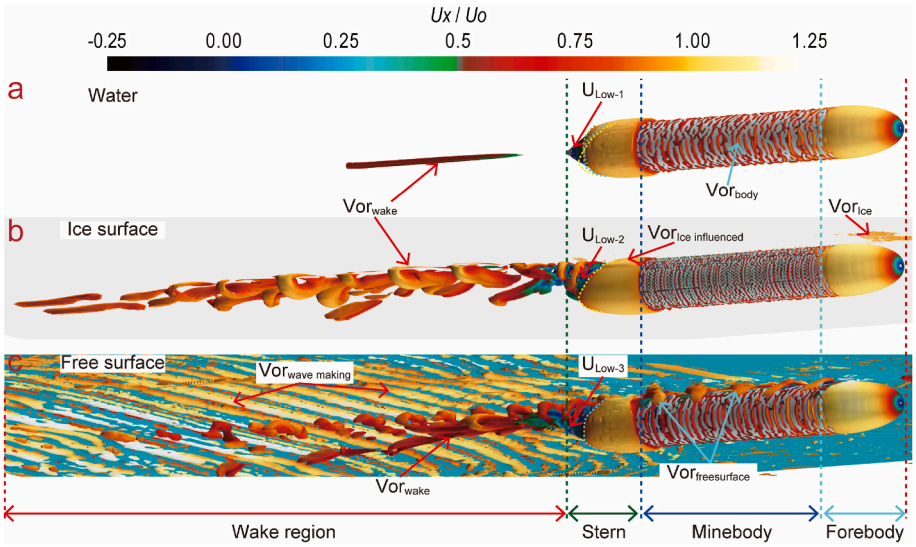

Fig. 20. Vortical structures around UUVs coloured with dimensionless velocity *Ux/U0* at the condition of (a) infinite depth, (b) near ice surface, and (c) near free surface.

Under different velocity conditions, the bound vortex structure of UUVs around the bow and stern area is extremely similar. The strip-shaped distribution of bound vortices in the middle body region of UUVs is wider and thicker with the increase in velocity. The range of vortices on the ice surface (Vor_{ice}) above the UUV increase with the velocity of UUV. Moreover, the ice-influenced vortex of the UUV ($Vor_{ice\ influenced}$) is more significant. The wake vortices under different velocity conditions are different in the wake region. When the velocity of the UUV is 0.5144 m/s, the shedding wake vortex of the UUV interacts with the ice surface, showing a hairpin vortex attached along the ice surface (Vor_{wake} and $Vor_{Hairpin}$). With the increase in velocity, the vortex system becomes regular, which is manifested as two symmetrical main vortex tubes. In the stern area of the UUV, the vortex structure will have a shedding and transitional region when it is separated from the UUV. When the velocity is 2.5722 m/s, the vortex tube is more stable, and has the strongest TKE (Fig. 16).

Fig. 23 shows vortical structures around the UUV coloured with dimensionless velocity U_x/U_0 at different diving depths near the ice surface with a velocity of 1.195 m/s. Fig. 23a and b shows aerial and lateral views of the vortical structures of the UUV, respectively.

As the diving depth increases, the influence of the wall effect on the vortex structure of the UUV gradually decreases, which is manifested in the gradual weakening of the axial and spanwise distribution range of the vortex structure in the wake region. When the diving depth is greater than 3D, the vortex structure distribution of the UUV is the same as that of infinite depth; the low-speed region at the stern area is also similar. Moreover, with the increase in diving depth, the adsorption effect of the free surface effect on the wake vortex decreases, and the oblique flow angle of the wake vortex gradually decreases, which is mutually confirmed with the LIC distribution in Fig. 19.

4.6. Pressure

Fig. 24 shows the UUV hull pressure distributions under different conditions with a velocity of 0.5144 m/s. Fig. 24a, b, and c depict the infinite depth, near ice surface, and near free surface conditions, respectively.

For the infinite depth condition, the pressure distribution of the UUV

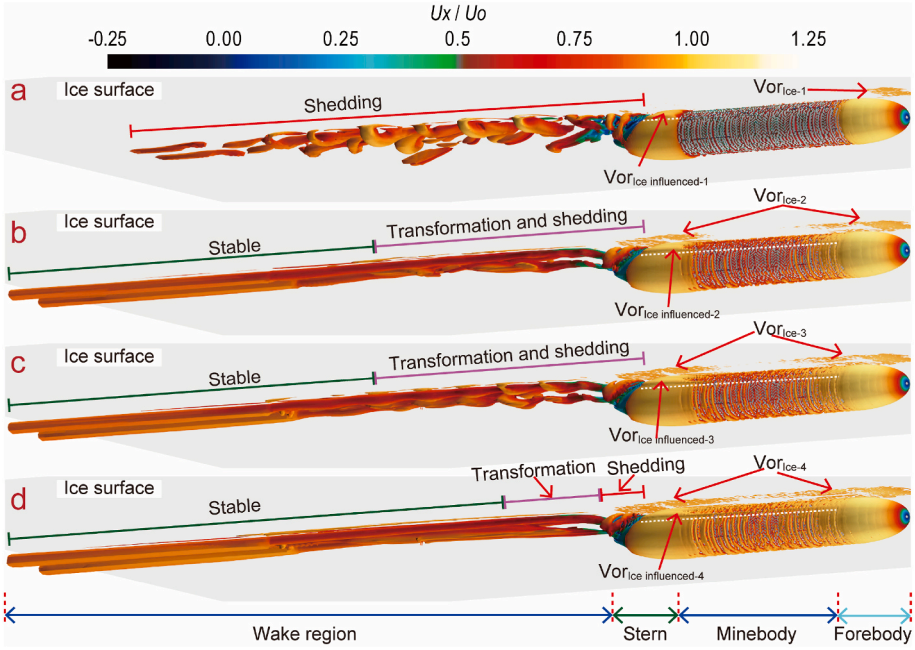

Fig. 21. Vortical structures around UUVs coloured with dimensionless velocity U_x/U_0 at different velocities near the ice surface: (a) V = 0.5144 m/s; (b) V = 1.195 m/s; (c) V = 1.5432 m/s; and (d) V = 2.5722 m/s.

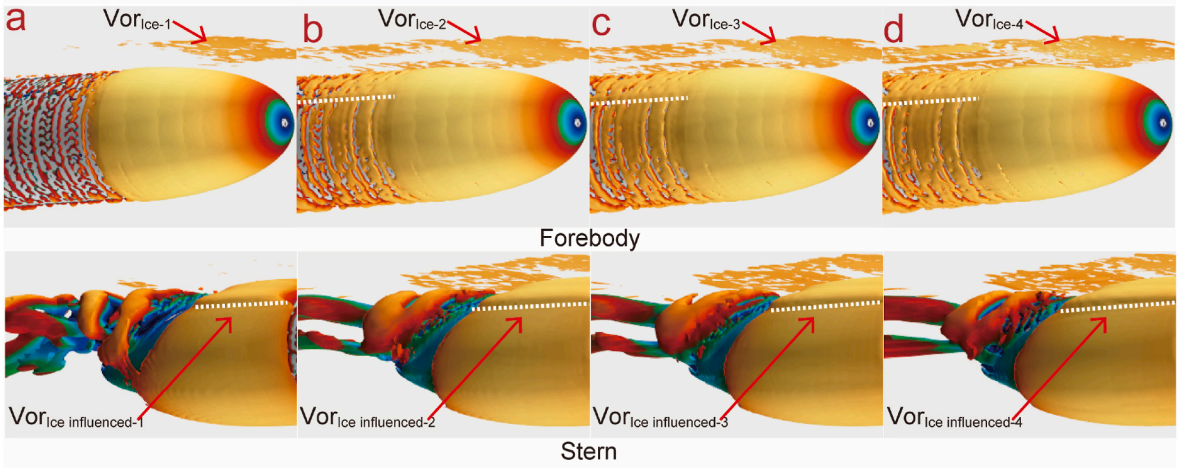

Fig. 22. Close-up of vortical structures around UUVs coloured with dimensionless velocity U_x/U_0 at different velocities near the ice surface: (a) V = 0.5144 m/s; (b) V = 1.195 m/s; (c) V = 1.5432 m/s; and (d) V = 2.5722 m/s.

is symmetrical, and there are negative pressure regions at the bow and stern areas ($P_{Negative\text{-}1}$ and $P_{Negative\text{-}4}$). For the near ice surface and free surface conditions, the pressure distribution of the UUV exhibits an asymmetric distribution. The range and amplitude of the negative pressure area in the bow area are larger than those in the infinite depth condition, which is shown as $P_{Negative\text{-}3} > P_{Negative\text{-}2} > P_{Negative\text{-}1}$ and $P_{Negative\text{-}6} > P_{Negative\text{-}5} > P_{Negative\text{-}3}$. Furthermore, owing to the interaction between the free surface and UUV, the free surface-influenced pressure distribution above the UUV is consistent with the phase of the transverse wave in free surface wave making ($P_{freesurface\ influenced}$). Fig. 24d and e shows the pressure distributions of the ice surface and free surface, respectively. The ice surface and free surface above the bow of the UUV show positive and negative pressure distribution characteristics, respectively ($P_{head\ influenced}$). In the near free surface condition, the pressure distribution is the same as the Kelvin waveform after the interaction between the UUV and free surface ($P_{wavemaking}$). Based on Bernoulli equation, the pressure in the area with high velocity is small. According to the comparison between pressure distribution of Fig. 24 and velocity distribution of Fig. 11, the high velocity area is consistent with the low pressure area.

Fig. 25 shows the UUV hull pressure distribution under the condition of near ice surface with different diving depths. Fig. 25-a, b, c, d, e, and f illustrate the diving depths of 0.625D, D, 2D, 3D, 5D, and infinite depth, respectively. When the diving depths are D and 2D, the UUV pressure distribution is asymmetric owing to the influence of the ice surface. When the diving depth is greater than 3D, the pressure distribution of the UUV is the same as that at an infinite depth.

Fig. 26 shows the ice surface pressure distribution under near ice surface conditions with different diving depths. Fig. 26a, b, c, d, e, and f show the diving depths of 0.625D, D, 2D, 3D, 5D, and infinite depth, respectively. It can be observed that, at different diving depths, the distribution of pressure in the bow and stern areas of the ice surface is different. With the increase in diving depth, the interaction and influence between the ice surface and UUV gradually decreases. At diving

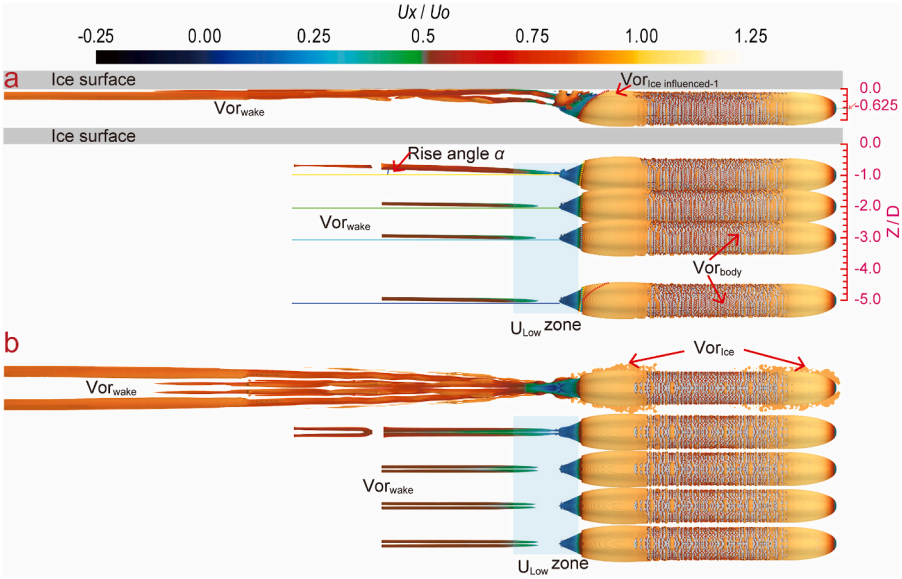

Fig. 23. Vortical structures around the UUV coloured with dimensionless velocity U_x/U_0 at different diving depths near the ice surface: (a) Lateral view and (b) Aerial view.

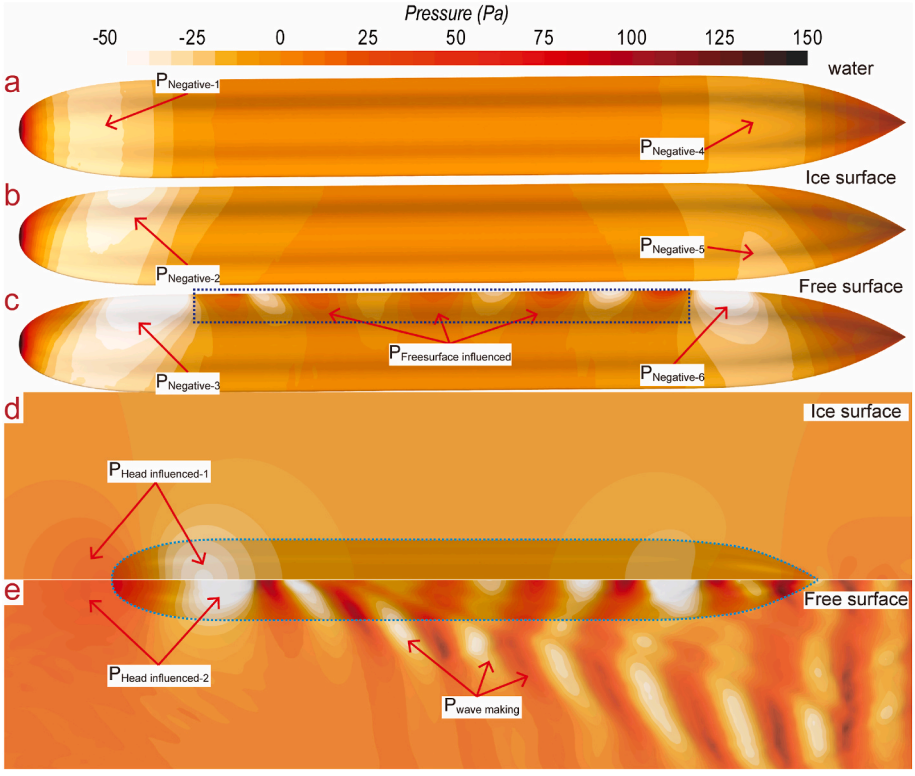

Fig. 24. Pressure distribution of the UUV hull, ice surface, and free surface. Hull pressure in (a) infinite depth condition, (b) near ice surface condition, and (c) near free surface condition. (d) Ice surface pressure. (e) Free surface pressure.

depths of 0.625D and D, there are positive and negative pressure distribution characteristics, respectively, above the UUV bow ($P_{head\ influenced}$). When the depth is greater than 2D, this pressure distribution characteristic disappears. With the increase in diving depth, the pressure distribution of the middle body-influenced ice surface also gradually decreases. When the diving depth is greater than 3D, the pressure distribution is the same as that at an infinite depth.

5. Conclusion

In this study, a numerical calculation was performed for UUV sailing at infinite depth, near free surface, and near ice surface conditions. Focusing on the effect of the ice surface on the performance of the UUV, the following conclusions are drawn from analysing the resistance coefficient, lift coefficient, velocity field distribution, and pressure in the hull.

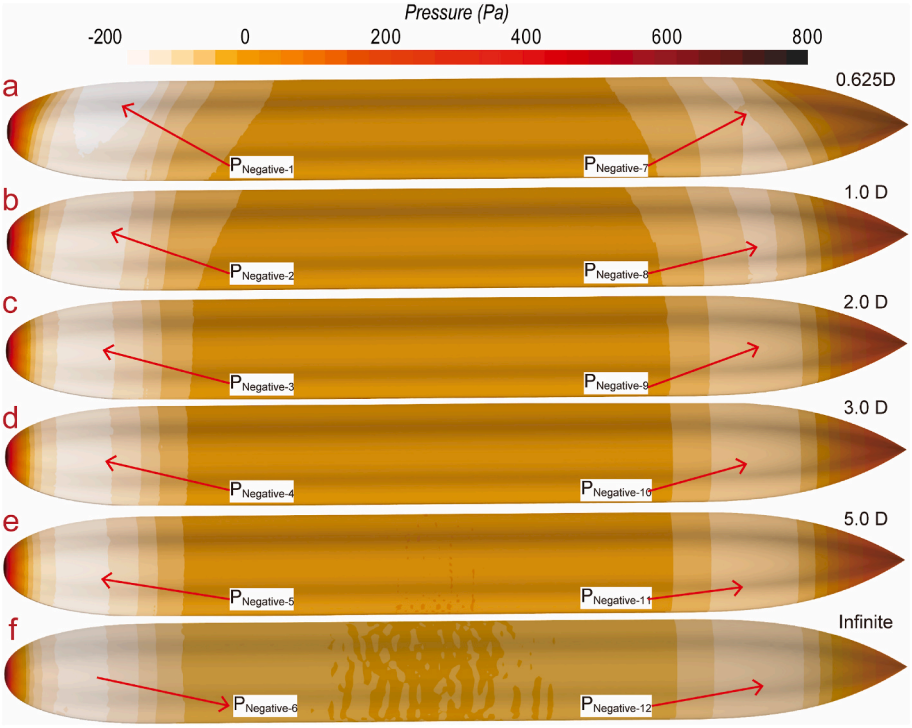

Fig. 25. Pressure distribution of the UUV hull under the condition of near ice surface with different diving depths: (a) 0.625D; (b) D; (c) 2D; (d) 3D; (e) 5D; and (f) Infinite depth.

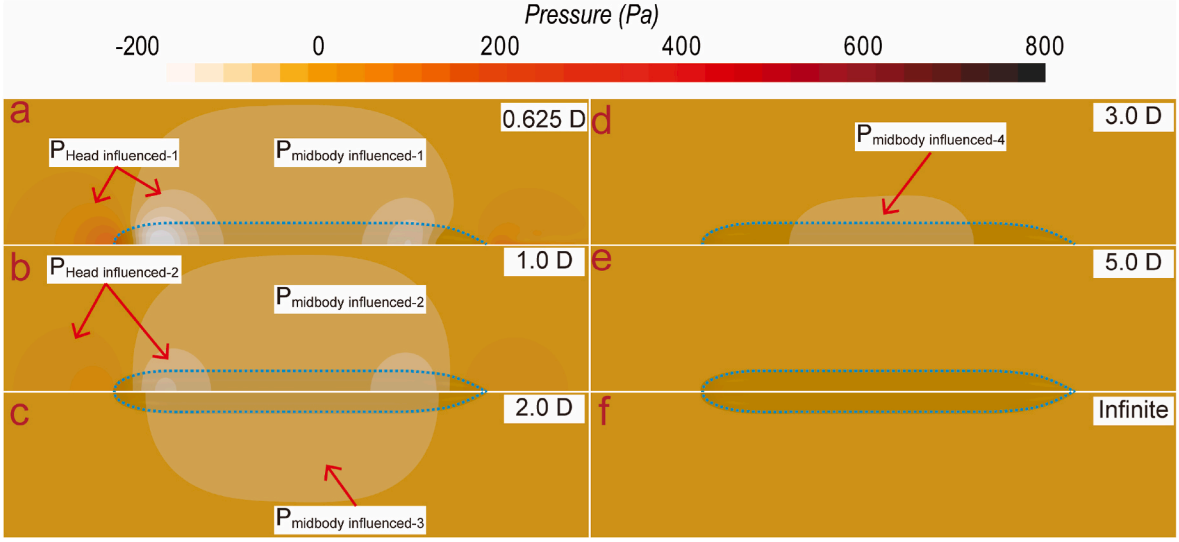

Fig. 26. Pressure distribution of the ice surface under the condition of near ice surface with different diving depths: (a) 0.625D; (b) D; (c) 2D; (d) 3D; (e) 5D; and (f) Infinite depth.

(1) The existence of ice surface makes the resistance coefficient different from that infinite depth and near free surface. The influence of ice surface on the resistance coefficient is related to the diving depth. The results show that, the effect of the ice surface and free surfaces on the resistance coefficient of the UUV can be neglected at diving depths greater than three times the diameter of the UUV.

(2) The lift coefficient when sailing near the ice surface is much larger than those at the corresponding velocities when sailing near the free surface and at infinite depth, indicating that the ice surface exerts an apparent upward suction effect on the UUV.

(3) The overall distribution of the velocity field when sailing near the ice surface and free surface is asymmetric, and the effect of ice on the velocity field is manifested by the appearance of a low-velocity zone in the stern region, the appearance of reflux, and shedding of eddies in the stern area. The effect of the ice surface on the velocity field distribution is not evident when the diving depth exceeds 3D, and can be neglected. The suction effect of the ice surface gradually increased with an increase in velocity.

(4) With the increase in diving depth, the influence of the wall effect on the vortex structure of the UUV gradually decreases. When the diving depth is greater than 3D, the vortex structure distribution of the UUV is the same as that under the infinite depth condition.

(5) When sailing near the ice surface, there are differences in the pressure of the bow and stern area at different diving depths, and a negative pressure area appears in both the bow and stern. The negative pressure at the stern area decreased with increasing diving depth.

Strictly speaking, the conclusion of this paper is valid for the UUV we selected in its specific working conditions. Different UUVs may have its corresponding conclusion according to its speed working condition and main scale parameters.

CRediT authorship contribution statement

Wanzhen Luo: Writing – original draft, Conceptualization, Methodology, Software, Funding acquisition, Resources. **Dapeng Jiang:** Writing – original draft, Validation, Writing – review & editing, Software, Visualization. **Tiecheng Wu:** Writing – original draft, Writing – review & editing, Methodology, Software, Visualization, Resources. **Moyu Liu:** Visualization, Writing – review & editing, Validation, Data curation. **Yulong Li:** Visualization, Writing – review & editing, Validation.

Declaration of competing interest

The authors declare that they have no known competing financial interests or personal relationships that could have appeared to influence the work reported in this paper.

Acknowledgements

This work was financially supported by the National Natural Science Foundation of China (grant no.52101379; 52101380); Natural Science Foundation of Guangdong Province, China (2021A1515012134); the Guangdong Basic and Applied Basic Research Foundation (2019A1515110721).

References

Alvarez, A., Bertram, V., Gualdesi, L., 2009. Hull hydrodynamic optimization of autonomous underwater vehicles operating at snorkeling depth. Ocean Eng. 36 (1), 105–112.
Alvarez, A., Caffaz, A., Caiti, A., Casalino, G., Clerici, E., Giorgi, F., Gualdesi, L., Turetta, A., Viviani, R., 2005. Folaga: a very low cost autonomous underwater vehicle for coastal oceanography. In: The Sixteenth IFAC World Conference, pp. 1–6.
Cabral, B., Leedom, L.C., 1993. Imaging vector fields using line integral convolution. In: Proceedings of the 20th Annual Conference on Computer Graphics and Interactive Techniques. August. Anaheim, California, pp. 263–270.
Cao, L.S., Huang, F.L., Liu, C., Wan, D.C., 2021. Vortical structures and wakes of a sphere in homogeneous and density stratified fluid. J. Hydrodyn. 33 (2), 207–215.
Guo, C.Y., Wu, T.C., Zhang, Q., Lou, W.Z., 2017. Numerical simulation and experimental studies on aft hull local parameterized non-geosim deformation for correcting scale effects of nominal wake field. Brodogradnja 68, 77–96.
Hirt, C.W., Nichols, B.D., 1981. Volume of fluid (VOF) method for the dynamics of free boundaries. J. Comput. Phys. 39, 201–225.
Hoerner, S.F., 1965. Fluid-Dynamic Drag: Practical Information on Aerodynamic Drag and Hydrodynamic Resistance. Washington DC.
Huang, S., Liu, W.Q., Luo, W.Z., Wang, K., 2021. Numerical simulation of the motion of a large-scale unmanned surface vessel in high sea state waves. J. Mar. Sci. Eng. 9 (9), 982.
Jagadeesh, P., Murali, K., Idichandy, V.G., 2009. Experimental investigation of hydrodynamic force coefficients over AUV hull form. Ocean Eng. 36 (1), 13–118.
Lee, S., Choi, H.S., Kim, J.Y., Paik, K.J., 2020. A numerical study on hydrodynamic maneuvering derivatives for heave-pitch coupling motion of a ray-type underwater glider. Int. J. Nav. Archit. Ocean Eng. 12, 892–901.
Liu, C., Gao, Y.S., Dong, X.R., Wang, Y.Q., Liu, J.M., Zhang, Y.N., Cai, X.S., N, G., 2019. Third generation of vortex identification methods: omega and Liutex/Rortex based systems. J. Hydrodyn. 31 (2), 205–223.
Mackay, M., 2003. The Standard Submarine Model: A Survey of Static Hydrodynamic Experiments and Semiempirical Predictions. Atlantic.
Mansoorzadeh, S., Javanmard, E., 2014. An investigation of free surface effects on drag and lift coefficients of an autonomous underwater vehicle (AUV) using computational and experimental fluid dynamics methods. J. Fluid Struct. 51, 161–171.
McPhail, S.D., Pebody, M., 1997. Autosub-1. A distributed approach to navigation and control of an autonomous underwater vehicle. In: Proceedings of the 7th International Conference on Electronic Engineering in Oceanography, pp. 16–22. Southampton, UK.
Menter, F.R., 1994. Two-equation eddy-viscosity turbulence models for engineering applications. AIAA J. 32 (8), 1598–1605.
Mitra, A., Panda, J.P., Warrior, H.V., 2019. The effects of free stream turbulence on the hydrodynamic characteristics of an AUV hull form. Ocean Eng. 174, 148–158.
Muzaferija, S., 1998. Computation of free surface flows using interface-tracking and interface-capturing methods. In: Nonlinear Water Wave Interaction. Computational Mechanics, Southampton, UK.
Perry, A.E., Chong, M.S., 1987. A description of eddying motions and flow patterns using critical-point concepts. Annu. Rev. Fluid Mech. 19, 125–155.
Polis, C., Ranmuthugala, D., Duffy, J., Renilson, M., 2013. Enabling the prediction of manoeuvring characteristics of a submarine operating near the free surface. In: Pacific 2013 International Maritime Conference: the Commercial Maritime and Naval Defence Showcase for the Asia Pacific, p. 281. Australia.
Ross, A., Fossen, T.I., Johansen, T.A., 2004. Identification of underwater vehicle hydrodynamic coefficients using free decay tests. IFAC Proc. 37 (10), 363–368.
Roy, C.J., Heintzelman, C., Roberts, S.J., 2007. Estimation of Numerical Error for 3D Inviscid Flows on Cartesian Grids. 45th AIAA Aerosp Sci Meet Exhib Aerosp Sci Meet., pp. 1–13. January.
Sahin, I., Crane, J.W., Watson, K.P., 1997. Application of a panel method to hydrodynamics of underwater vehicles. Ocean Eng. 24 (6), 501–512.
Shariati, S.K., Mousavizadegan, S.H., 2017. The effect of appendages on the hydrodynamic characteristics of an underwater vehicle near the free surface. Appl. Ocean Res. 67, 31–43.
Sharma, S., Jesudhas, V., Balachandar, R., Barron, R., 2019. Turbulence structure of a counter-flowing wall jet. Phys. Fluids 31 (2), 025110.
Smits, A.J., Lim, T.T., 2012. Flow Visualization, Techniques and Examples. IMPERIAL COLLEGE PRESS, London. https://doi.org/10.1142/p808.
Spalart, P.R., 2009. Detached-eddy simulation. Annu. Rev. Fluid Mech. 41, 181–202.
Vine, A.J., Renilson, M.R., Gottschalk, S.A., 1991. An Investigation into the Drag Forces Acting on a Submerged Hull Travelling Close to a Free Surface. Australian Maritime College, Launceston.
Wang, L.Z., Wu, T.C., Gong, J., Yang, Y.R., 2021. Numerical simulation of the wake instabilities of a propeller. Phys. Fluids 33, 125125.
Weinblum, G., Amtsberg, H., Bock, W., 1950. Tests on Wave Resistance of Immersed Bodies of Revolution. David Taylor Model Basin, Washington DC.
Weinblum, G., Blum, J., 1951. The Wave Resistance of Bodies of Revolution. David Taylor Model Basin, Washington DC.
Wilson-Haffenden, S., Renilson, M., Ranmuthugala, D., Dawson, E., 2010. An investigation into the wavemaking resistance of a submarine travelling below the free surface. In: International Maritime Conference 2010: Maritime Industry-Challenges, Opportunities and Imperatives, p. 495. Sydney, Australia.
Zhao, W.W., Wang, Y.Q., Chen, S.T., Ma, C.H., Wan, D.C., 2021. Parametric study of Liutex-based force field models. J. Hydrodyn. 33 (1), 86–92.